4.3 DUCTILE PHASE TOUGHENING OF 90-97wt% W-NiFe HEAVY METAL ALLOYS—M.E. Alam, S. Pal, K. Field, G. R. Odette (UCSB)

OBJECTIVE

The objective of this research is to develop W-Ni:Fe and other heavy metal W alloys as ductile phase toughened composites for the fusion reactor divertor applications.

SUMMARY

Ductile phase toughening (DPT) is a promising approach to improving toughness of brittle materials like tungsten (W). The fracture toughness of commercial liquid phase sintered W-based composites, containing 90, 92.5, 95 and 97 wt.% W, with the balance a 7:3 Ni:Fe ductile solid solution phase, has been characterized. Pre-cracked single edge notch bend bar fracture toughness tests were conducted at room temperature. The average maximum load initiation toughness averaged 102 ± 17 MPa√m, relatively independent of the W fraction up to 95 wt.%, but dropped to 71± 17 MPa√m for the 97%W alloy. However, crack blunting beyond the peak load (down to $P/P_{max} \approx 0.8$), prior to any significant crack growth (da), resulted in an even higher toughness of 168 ± 31 MPa√m. The toughness of the W-Ne:Fe composites compare to typical monolithic-W values of ≈ 8 MPa√m. Composite fracture occurs by stable crack growth. The enormous toughening is due to crack bridging and especially very large plastic zone deformation energy dissipation.

PROGRESS AND STATUS

Introduction

Tungsten (W) is the leading candidate for plasma facing component of the future fusion reactor divertor applications due to its high melting temperature, good conductivity, low sputtering rates and high temperature strength [1-2]. However, an elevated brittle to ductile transition (BDT) temperature and low toughness (and ductility), which are further degraded by neutron irradiation, limit W's application as structural material. One promising approach to toughening is to include ductile phases (DP) in ta W-composite to restrict crack propagation by crack bridging and deflection mechanisms, as well as to provide energy dissipating crack tip plastic deformation processes. Both bridging and crack tip plastic deformations increase the toughness and lower the composite BDT [3]. Tungsten heavy (metal) alloys (WHAs), or composites, typically consist of 78-98 wt.% W and other ductile phase separated elements like Ni, Fe, Cu, Co, Cr. They have been studied for several decades. Most of this research has focused on processing optimization and relating the WHA microstructure to tensile properties. Surprisingly, only very few studies have been conducted on the fracture toughness of WHA's [4]. Following previous work carried out at PNNL, in collaboration with UCSB, we carried out room temperature fracture toughness tests of W-Ni:Fe WHA with 90 to 97 wt.%W. Complementary microstructural, hardness and tensile tests were also conducted.

Experimental Procedure

Four commercially available (Mi-Tech Metals, Indianapolis, In, USA) liquid-phase sintered W-Ni:Fe composites with 90, 92.5, 95 and 97 W (wt.%) and balance 7:3 Ni:Fe (see Table 1) were studied. Note it is very important to emphasize that these WHA are composed of a small volume fraction of a semi-continuous Ni:Fe fcc solid solution ductile phase, surrounding a much higher volume fraction of large W-particles. The WHA's were received in the form of 100mmx100mmx14mm plates. The specimens for the different tests were fabricated using electro-discharge machining (EDM). They were ground with to 2000 grit sand paper to remove EDM damage and residual surface stresses. Some fracture specimen sides were then polished down to 0.5µ-diamond paste, and etched in a 30% hydrogen peroxide solution for 10min to facilitate microstructural characterization. Scanning electron microscopy (SEM) with energy dispersive spectroscopy (EDS), and electron backscatter diffraction (EBSD), were used to image W particles and the surrounding Ni:Fe phase, and to identify their respective compositions.

Vickers microhardness measurements were performed on the polished surfaces at a 500g load using a LECO M-400A semi-automated hardness tester, and the reported values are based on the average of 10

to 15 indents. Nanoindentation (TriboIndenter, Hysitron Inc., MN, USA) with a Berkovich tip was used to measure the reduced elastic modulus (E_r) and the nanohardness (NH) of W and Ni:Fe phases under a 10mN loading cycle: 10s ramp loading, 10s dwell and 10s unloading. The unloading curve was used to characterize E_r. Room temperature tensile tests were performed on EDM fabricated flat dog-bone shaped sub-sized specimens with a gauge section length x width x thickness of 5.0x1.2x0.5 mm^3. The tensile specimens were sanded with 1500 grit to remove minor defects and surface residual stresses due to EDMing. The tests were carried on an 810 MTS servo-hydraulic universal load frame with a 956 controller. Tensile loading was at a crosshead speed of 0.30 mm/min, corresponding to a strain rate of $\approx 10^{-3}$/s; crosshead displacement was used to measure strain and the corresponding tensile ductility parameters.

Room temperature fracture toughness test were conducted on fatigue pre-cracked single-edged notch three-point (3PB) and four-point bend (4PB) bend specimens with nominal length x width x thickness dimensions of 16x3.3x1.65 mm^3. Pre-cracking and fracture testing were also carried out on the 810 MTS servo-hydraulic load frame. The specimens were pre-cracked to a nominal crack length (a)-to width (W) ratios, (a/W), from 0.3 to 0.5. To facilitate in-situ optical observation of the crack tip region, the fracture specimen sides were sanded with a sequence of 2000 grit, 9µ, 3µ and 1µ papers. Initially 4PB tests were conducted, in part to help control possible unstable crack growth. However, since the crack growth was found to be highly stable, subsequent fracture testing was based on a 3PB fixture. The fracture tests were carried out at a crosshead speed of 0.04mm/min. ASTM C1421 and ASTM E1921 were used to calculate the elastic and plastic components of the fracture toughness, respectively, for the 4PB tests. ASTM E1921 was used to evaluate both the elastic and plastic components of fracture toughness for the 3PB tests. The K_{Jc} were calculated at the maximum load (P_m) in the load-displacement (P-d) curve. K_{Jc} were also evaluated at loads down to ≈ 80% of P_m, since there was minimal crack growth (< 200 µm) for the displacements up to this loading point. The 4PB tests were carried out down to very low P, involving extensive crack tearing to near the back of the specimen. The 3PB tests were stopped at P/Pm of 0.77 to 0.92 to better evaluate an initiation toughness and corresponding crack tip opening displacement (CTOD). The pre-crack and crack lengths were also measured after the specimens were broken in LN_2.

Table 1. Chemical compositions (wt.%) of the W-Ni:Fe alloys

WHA	W	Ni	Fe	Ductile phase (DP) area fraction (%)	DP compositions: Ni/W/Fe
90W	90.27	6.78	2.95	21.4	51.2/28.5/20.3
92.5W	92.48	5.33	2.19	14.9	49.1/31.3/19.6
95W	95.03	3.48	1.49	12.3	49.1/32.2/18.7
97W	97.13	2.01	0.86	9.3	48.3/34.3/17.4

Results

Microstructure

SEM micrographs of the polished and etched W-N:iFe plates shown in Figure 1 reveal roughly spheroidal W particles surrounded in the interconnected skeleton of a ductile Ni:W:Fe phase. An EDX scan shows that the particles are close to 100% W, while the Ni:W:Fe phase is approximately 50%Ni, 30%W and 20%Fe. The fraction of W in the Ni:W:Fe phase increases slightly from 28.5 wt% to 34.3 wt% with increasing WHA W (Table 1). Figure 1 also shows the W–particle size increases from ≈ 18 µm for 90W-Ni-Fe alloy to ≈ 38 µm for 97W-Ni-Fe alloy (Table 2 and Figure 1). The increase in the W-particle size permits maintaining a similar Ni:W:Fe ductile phase (DP) skeleton web thickness with an increasing fraction of W. This may be an important alloy design consideration in developing WHA with more than 97% W. Of course the area fraction of the Ni:W:Fe phase decreases with higher W. Shapes of the particles are generally spheroidal up to 95W alloys, and become slightly more polyhedral at 97W. A higher W fraction lowers the Ni:W:Fe phase continuity and increases the W-W contiguity and particle bonded W-W interfaces. Note the 95W WHA contains some cracked W particles (red arrows in Figure

1c), although the reason for this is not known. Figure 2 shows the EBSD inverse pole figure (IPF) maps for the 90W alloy, indicating random orientations of the W particles. Some large particles show multiple textures in a single particle that are likely due to multiple grains or subgrains at the larger size.

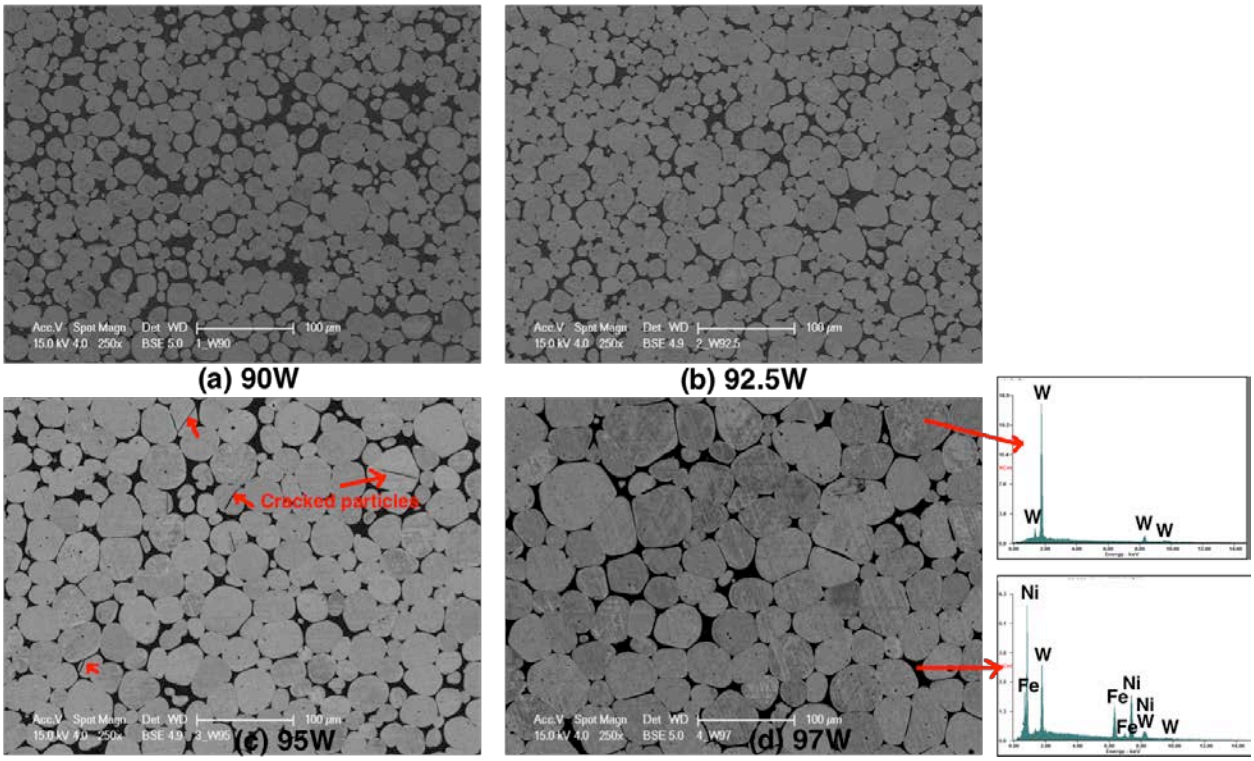

Figure 1. SEM images show the spheroidal W-particle and matrix of: (a) 90W, (b) 92.5W), (c) 95W, and (d) 97W, respectively. EDX images show the 99+% pure W particles embedded in Ni-rich Ni-W-Fe matrix.

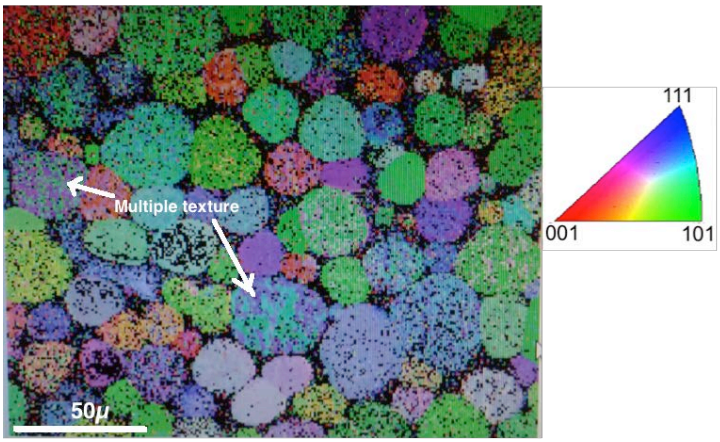

Figure 2. EBSD IPF maps show random texture, in general, with multiple textures in some large particles.

Nanoindentation and Microhardness

Table 2 shows the reduced elastic modulus (E_r) of W-particles and Ni:W:Fe phase for all four alloys. The average modulus of elasticity varies from 378 to 428 GPa for W-particles and 259 to 296 GPa for the Ni:W:Fe phase. The highest E_r is in the 95% W alloy. Nanohardness (NH) was also calculated from the indentation loading-unloading curves. The 95W alloy also shows the highest hardness of 7.2GPa, while the Ni:W:Fe phase shows the lowest hardness of ≈ 4.3 GPa. Vickers microhardness (H_v) data for the W-alloys are also summarized in Table 2. While the hardness varies between 321 (90%W) to 349 kg/mm^2 for all the W alloys, the 95W alloy again shows the highest H_v.

Table 2. Particle size, modulus of elasticity and hardness of WNiFe alloys

Code name	Particle size (µm)	Er (GPa)		Nano-H (GPa)		µ-H (Hv), kg/mm^2
		W-particle	Matrix	W-particle	Matrix	
90W	18 ± 7	397 ± 17	269 ± 20	7.0 ± 0.3	5.3 ± 0.2	321 ± 9
92.5W	18 ± 7	378 ± 12	268 ± 18	5.8 ± 0.2	4.8 ± 0.1	334 ± 8
95W	27 ± 11	428 ± 8	296 ± 31	7.2 ± 0.4	4.3 ± 0.2	349 ± 7
97W	38 ± 15	394 ± 29	259 ± 12	6.3 ± 0.6	4.9 ± 0.2	344 ± 9

Tensile Properties

Figure 3 shows the engineering stress-strain s(e) curves along with macroscopic fracture surface from room temperature tensile tests on the W-Ni:Fe alloys. The s(e) curves are generally similar, although the total elongation systematically decreases with increasing W. Significant strain hardening is observed in all cases. The tensile data are summarized in Table 3. The 0.2%-offset yield stress (s_y) does not vary significantly with W. However, ultimate tensile stress (s_u), uniform (e_u) and total (e_t) elongations, and reduction in area (RA) of the neck decrease with increasing W; and there is a noticeable strength and ductility drop off between 95 and 97%W. Fracture in these alloys takes place almost immediately after reaching ultimate tensile stress. Macroscopic fracture surfaces shows minimal necking, expect for 90W alloy, reflected in their lower RA value.

Table 3. Room temperature tensile properties of W-Ni:Fe alloys

Code name	s_y (MPa)	s_u (MPa)	s_y/s_u	e_u (%)	e_t (%)	Hardening exponent, n	RA (%)
90W	621 ± 29	891 ± 35	0.70	18 ± 4	21 ± 7	0.094	25.8
92.5W	616 ± 44	886 ± 12	0.70	13.5 ± 2.2	16 ± 4	0.099	13.1
95W	600 ± 15	818 ± 10	0.73	7.3 ± 1	8 ± 1	0.102	9.3
97W	594 ± 27	701 ± 67	0.85	3.4 ± 1	4 ± 0.7	0.071	6.2

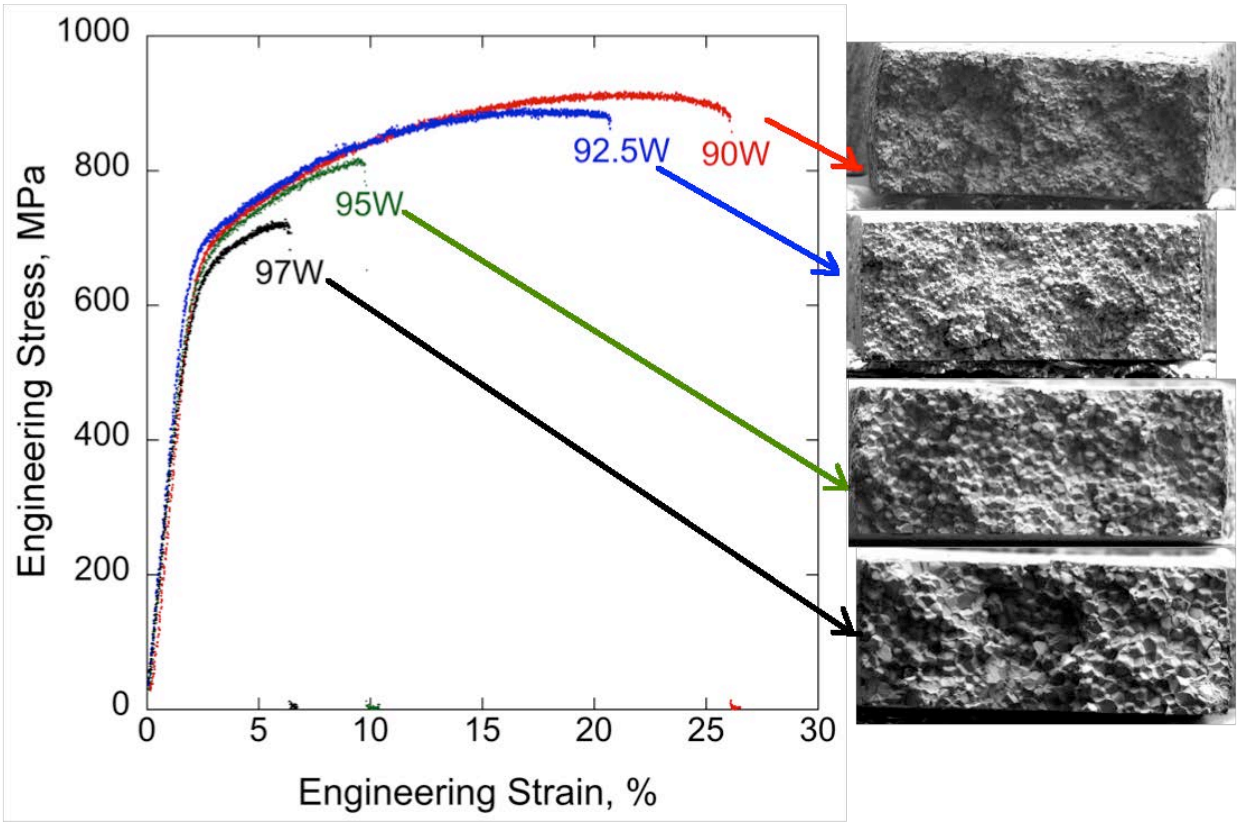

Figure 3. Room temperature engineering stress-strain curves, and their corresponding macroscopic view of fracture surface for the W-Ni:Fe alloys.

The W-Ni:Fe alloys manifest four local failure modes, namely: W-W intergranular fracture (WW), W cleavage (WC), W-Ni:W:Fe phase interfacial separation (WM), and Ni:W:Fe ductile phase rupture (MR) [4-5]. SEM micrographs of the fracture surfaces of the broken tensile specimens, shown in Figure 4, illustrate all of these failure modes. The W-W interfacial boundary is the weakest, and the W-W interfacials are increases with increasing W (see Figure1). Specimen fracture initiates by WW at the W-W particle interfaces, and continues by crack propagation though the W-Ni:W:Fe phase accompanied by W cleavage. Figure 4 shows that the fraction of WC is highest for 90W, and minimal for 97W alloys that experience more WW separation. Notably, WC appears to correlate with higher strength and ductility (see Table 3).

Fracture Toughness

Room temperature fracture toughness tests were conducted on the single-edge notched fatigue pre-cracked bend bars using both 4PB and 3PB fixtures. The fatigue crack tends to mainly propagate through the Ni:W:Fe ductile phase (white arrow, Figure 5a). The pre-cracked specimens were heat tinted at 400ºC for 1 min to mark the pre-crack front (Figure 5b). Some specimens were also speckled with graphite powders in an attempt to use *in-situ* digital image correlation (DIC) to measure the crack length during loading in the 4PB test. However, it turned out that DIC was not possible due to the large lateral contraction (Figure 5b) in the extensive crack tip plastic zone, which optically image as dark area in Figure 5c. SEM images shows that the fracture crack growth under pseudo-static loading is mainly transgranular (red arrow, Figure 5d).

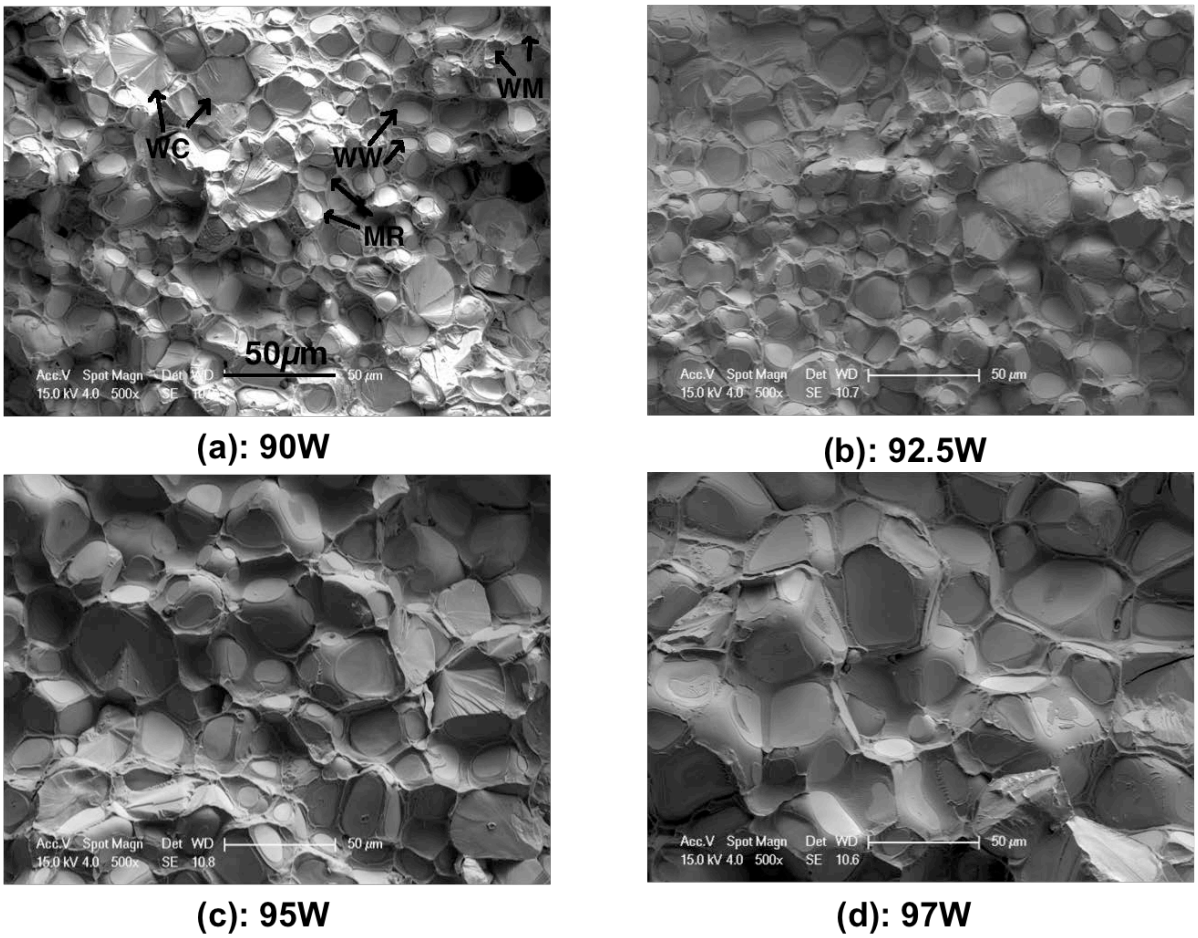

Figure 4. SEM fractographs of the room temperature tensile fracture surfaces for different WNiFe alloys.

Normalized load-displacement (P-d) curves for the W-Ni:Fe alloys, shown in Figure 6a, reveal continuous load drop after P_m with increasing d, indicating stable crack growth even at room temperature. The normalization involves adjusting the actual P-d data to a common a/W = 0.5, so that the curves can be inter compared. The peak loads are similar except for the 95% W alloy where P_m is higher. Substantial strain hardening is also observed in all alloys except for the 97W WHA (Figure 6a), consistent with the corresponding tensile s(e) curves. The shapes of the post-max P-d curves are generally similar. Since 4PB tests show massive stable crack growth, additional tests were conducted on very finely ground (down to 1μ sandpaper) specimens in the 3PB fixture, and the crack tip region was observed *in-situ* with an optical microscope. These tests were stopped at a P/P_{max} from ≈ 0.77 to 0.92 (Table 4). Unfortunately, the lateral contraction (surface dimpling), marked by the dark areas in Figure 6b, prevented imaging the crack tip. However, post-test SEM examinations show that there was very little crack growth (< 200 μm) at these P/P_m loads. Thus additional crack blunting, and the corresponding increase in the CTOD, is actually associated with the initiation toughness, rather than a classical J-da R-curve behavior. Thus the toughness versus P/P_{max} for all W alloys was calculated, showing that the toughness increases significantly with decreasing P/P_{max} (Figure 6c). Figure 6d shows the calculated K_{Jc} at P_m and P/P_m ≈ 0.8 for all 4 alloys and these results are tabulated in Table 4.

The K_{Jc} do not show a systematic trend with the W loading. K_{Jc} is highest in the 95W alloy and lowest for 97W. The slightly higher toughness of 95W might be due to the combination of: a) the presence of cracked W-particles in as-received condition; b) the higher modulus of elasticity of W-particles and the Ni:W:Fe ductile phase; and c) higher hardness of the alloy and W phase. The lower K_{Jc} in the 97W may be due to increased W-W contiguity. Most notably, however, even a minimal ductile phase content of ≈ 3 wt.% increases the room temperature initiation toughness relative to pure W between 9 and 18 times. Initiation is followed but extremely stable crack growth, and very high effective ductility. Detailed experimental and modeling studies of the toughening mechanisms illustrated in Figure 7 in the W-Ni:Fe WHA will be reported in the future.

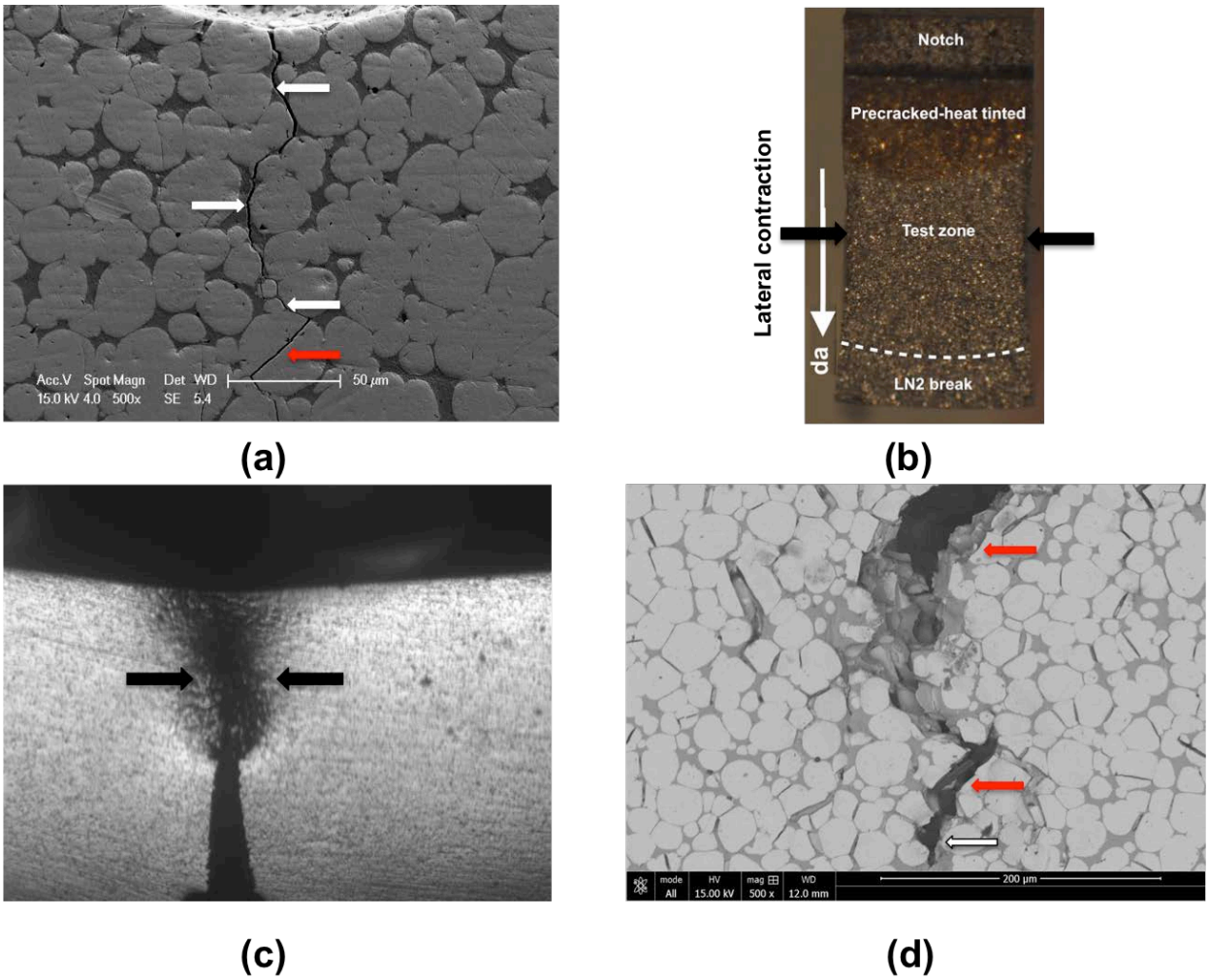

Figure 5. (a) SEM image shows the fatigue crack path mainly propagate through the matrix phase (white arrows), (b) different zones of the specimen, (c) *in-situ* optical image shows large dark area due to lateral contraction of the plastic process zone, and (d) transgranular crack propagation (red arrows) during static loading.

Table 4. Crack and toughness statistics of WNiFe alloys.

Code	Sp. ID	Crack and toughness							CTOD (μm)	Fixture
		a_i(μ)	a_i/W	**K_{Jc} (MPa√m)**	a_f(μ)	P_f/P_{max}	K_{Jf} (MPa√m)	Δa (μ)		
90W	W1-1	1291	0.389	**94.7**	2260	0.173	330.7	969	220	4PB
	W1-2	1076	0.323	**93.8**	2090	0.27	305.1	1014	310	4PB
	W1-5	1553	0.466	**125.5**	1657.4	0.818	193.4	104	46	3PB
	W1-6	1091	0.326	**78.4**	1174	0.778	158.1	83	24	3PB
	Avg:			**98 ± 20**						
92.5	W2-1	1344	0.404	**99**	2672	0.22	405	1328	243	4PB
	W2-2	1415	0.424	**94.9**	1440	0.915	135	25	16	4PB
	W2-3	1236	0.372	**101.5**	1387	0.80	154.7	67	26	3PB
	W2-6	1306	0.393	**85.2**	1368	0.802	144.6	62	34	3PB
	Avg:			**95 ± 7**						
95W	W3-1	1761	0.531	**115.6**	2501	0.281	313.4	740	209	4PB
	W3-2	1020	0.306	**121.9**	1286	0.779	227.9	266	82	4PB
	W3-3	1240	0.370	**84.4**	1410	0.816	193.4	170	22	3PB
	W3-5	1477	0.441	**126.2**	1619	0.793	192	142	56	3PB
	Avg:			**112 ± 19**						
97W	W4-1	1155	0.348	**51.2**	2781	0.209	373.61	1626	233	4PB
	W4-5	1212	0.366	**80.5**	1403	0.793	148.2	191	43	3PB
	W4-6	1271	0.383	**80.4**	1362	0.767	136.6	91	44	3PB
	Avg:			**71 ± 17**						

Note: a_i= initial crack length; a_f=final crack length; K_{Jc}= toughness at maximum load; K_{Jf}=toughness at final crack length; P_{Jf}/P_{max}= load at final crack to maximum load; Δa=crack extension, a_f-a_i; and CTOD= crack tip opening displacement.

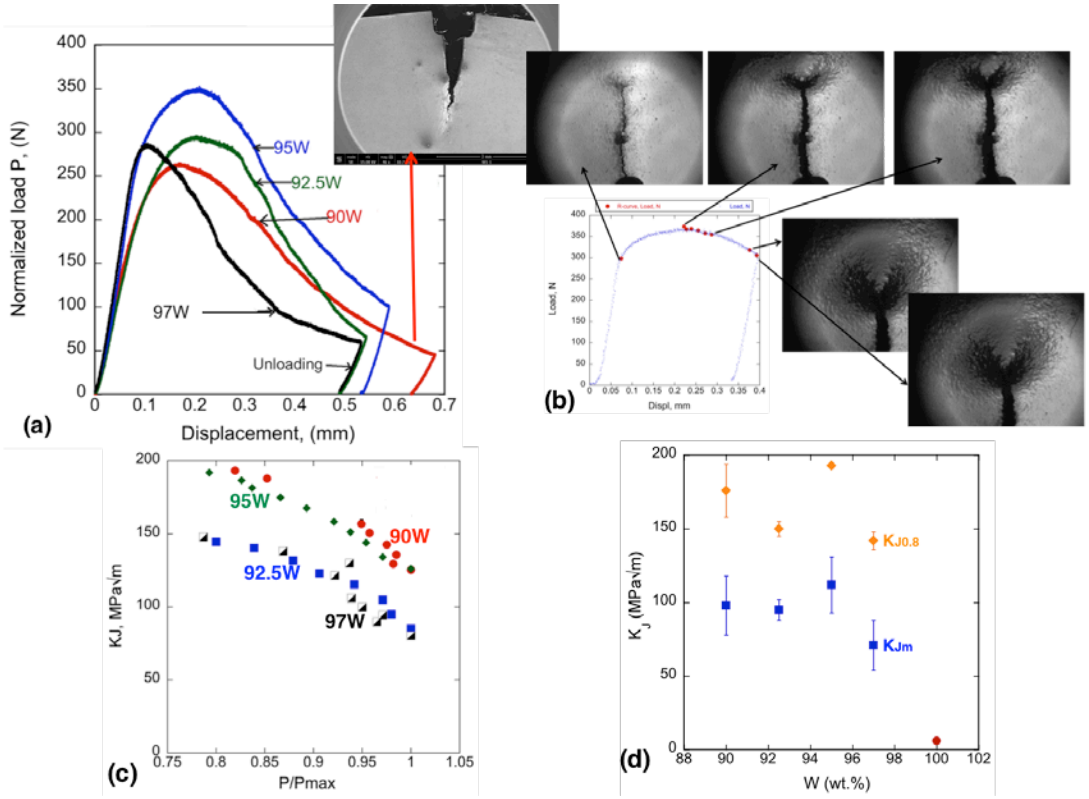

Figure 6. (a) Normalized P-D curves to a/W=0.5 tested at room temperature; insert image shows ductile tearing for 90W alloy, (b) P-D curve for a 92.5W alloy, corresponding with *in-situ* optical images, (c) K_J vs P/P_{max} of WNiFe alloys for 3PB test, and (d) average fracture toughness, K_{Jm} and $K_{J0.8m}$ of WNiFe alloys at P_{max} and P/P_m ≈0.8, respectively. Crack extension, da was less than 200μm for P/P_m ≈0.8.

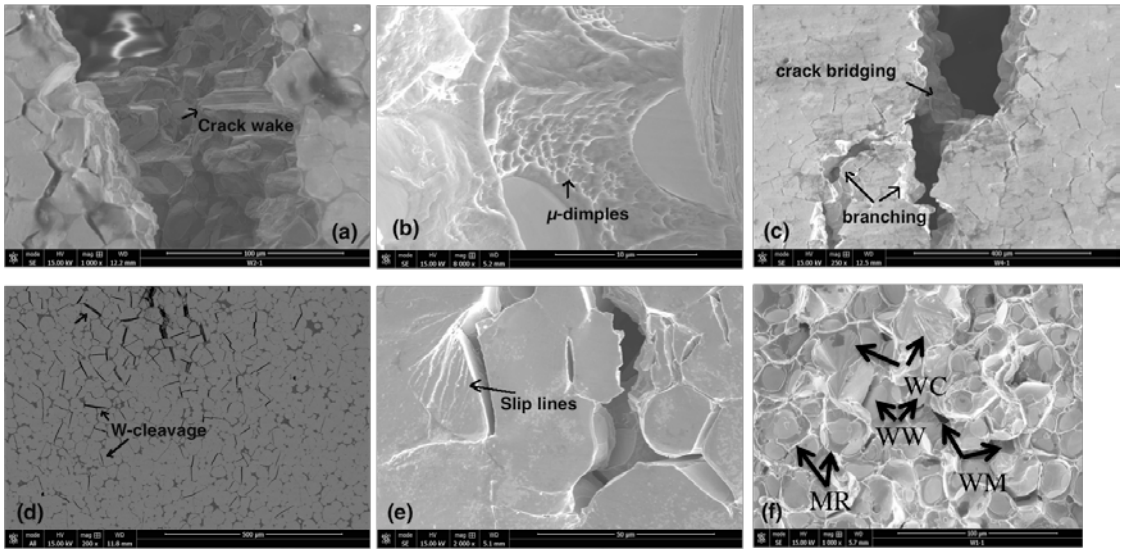

Figure 7. Series of SEM images show: (a) crack wake bridging, (b) formation of micro-dimples in NiWFe phase, (c) crack bridging and crack branching, (d) massive process zone near the crack tip plasticity and tungsten cleavage, (e) slip plane in W-particles, and (f) local fracture modes.

Room temperature fracture toughness measurements on four 90-97 wt.% W-Ni:Fe alloys showed that the initiation toughness is on the order at least 9 to 18 times that of typical the monolithic W (8 MPa√m). Extremely stable crack growth is observed for all alloys. Multiple toughening mechanisms include crack wake bridging, micro-cracking, micro-crack bridging, crack deflection, and especially extensive process zone plasticity.

In the future these initial studies will be extended to characterizing and modeling the detailed toughening mechanisms, higher and lower temperature testing, in situ XRD deformation studies and fabrication of hybrid model divertor components.

References

[1] K. H. Cunningham, K. Fields, D. Gragg, F. W. Zok, C. H. Henager, Jr, R. J. Kurtz, and T. Roosendaal, Recent Progress in the Development of Ductile-Phase Toughened Tungsten for Plasma-Facing Materials, in DOE/ER-0313/54 - Volume 54, Semiannual Progress Report, June 30, 2013. 2013, US DOE: ORNL, TN.

[2] C. H. Henager, Jr, R. J. Kurtz, T. J. Roosendaal, B. A. Borlaug, G. R. Odette, K. H. Cunningham, K. Fields, D. Gragg, and F. W. Zok, Recent Progress in the Development of Ductile-Phase Toughened Tungsten for Plasma-Facing Materials, in DOE/ER-0313/55 - Volume 55, Semiannual Progress Report, Dec. 31, 2013. 2013, US DOE: ORNL, TN.

[3] C.H. Henager, E. L. Stevens, R.J. Kurtz, T.J. Roosendaal, E.A. Nyberg, CA Lavender, GR Odette, KH Cunningham, and FW Zok, “Recent Progress in the Development of Ductile-Phase Toughened Tungsten for Plasma-Facing Materials: W-Ni-Fe Composites”, in DOE/ER-0313/58 - Volume 58, Semiannual Progress Report, June 30, 2015.

[4] KMO Zamora, JG Sevillano, MF Perez, “Fracture toughness of W heavy alloys”, Materials Science and Engineering A, 157 (1992) 151-160.

[5] ZH Zhang, FC Wang, SK Li, L Wang, “ Deformation characteristics of the 93W-4.9Ni-2.1Fe tungsten heavy alloy deformed by hydrostatic extrusion”, Mater Sci Engr A 435-436 (2006) 632-637.